Supplementary Information for

Non-Invasive Salivary Nicotine Detection for Oral Cancer Risk Assessment Using a Point-of-Care Electrochemical Device Functionalized with Carbon@MXene/Au Nanocomposite

Authors:

Monika Kumari[a], Lakahn Kumar[a], Sneh Sharma[b], Pawan Gupta[c], Ravi Kumar Arun[a*]

Affiliations:

[a] Department of Chemical Engineering, Indian Institute of Technology, Jagti, NH-44, Jammu-181221, India.

[b] School of biotechnology, Shri Mata Vaishno Devi university,182320, India.

[c] MAX Institute of Cancer Care - East Zone, MAX Super Specialty Hospitals, 201012, India.

SI. 1. Synthesis of Gold-nanoparticles (AuNPs)

Gold nanoparticles (AuNPs) were synthesized via the reduction of tetrachloroauric acid trihydrate ($HAuCl_4$) (Merck, Germany). using trisodium citrate (Merck, Germany) as a reducing agent in a modified Turkevich method.[1] Initially, 6 mg of trisodium citrate was dissolved in 1 mL of deionized water, and the solution was stored under refrigeration for later use. Separately, 500 µL of 0.01 M chloroauric acid ($HAuCl_4$) solution was added to 10 mL of boiling deionized water, stirred continuously. Once the gold precursor was fully mixed, the pre-prepared trisodium citrate solution was added dropwise to the boiling solution. The reaction mixture was kept under constant stirring, during which a noticeable color change occurred—from pale yellow to deep red, indicating the successful formation of gold nanoparticles.

SI. 2. UV-VIS and FTIR characterization

UV-VIS spectroscopy was employed to confirm the formation of the MXene/Au nanocomposite using a Carry 60 spectrophotometer (Agilent, USA). The pristine MXene dispersion exhibited a strong absorption feature at ~275 nm, as shown in Fig. S2, consistent with the previously reported optical responses of few-layer MXene sheets.[2] Citrate-stabilized Au nanoparticles exhibited a characteristic localized surface plasmon resonance (LSPR) peak at ~520 nm.[1] Upon integration of AuNPs with MXene, the spectrum showed a broadened and red-shifted plasmon band centered at ~553 nm, accompanied by retention of the MXene UV band. This red shift and band broadening indicate strong plasmon support interactions and changes in the local refractive index around AuNPs, confirming successful decoration of $Ti_3C_2T_x$ nanosheets with Au and the formation of the MXene/Au hybrid structure.[2,3]

Fourier transform infrared (FTIR) spectroscopy was employed using a Thermo Scientific Nicolet iS5 spectrometer (Thermo Fisher Scientific, USA) to investigate the surface chemistry and functional groups of pristine MXene and the MXene/Au nanocomposite (Fig. S3). The FTIR spectrum of MXene exhibits a broad absorption band in the range of 3200–3500 cm^{-1}, which is attributed to O–H stretching vibrations arising from surface hydroxyl groups and intercalated water molecules.[4,5] This feature is characteristic of $Ti_3C_2T_x$ MXene and reflects the presence of hydrophilic surface terminations. The absorption band observed in the region of 2350–1650 cm^{-1} corresponds to C=O stretching and O–H bending vibrations, indicating partial surface oxidation and the presence of interlayer water.[4] Additional bands appearing in the range of 1450–1350 cm^{-1} are associated with Ti–OH bending modes, confirming the presence of hydroxylated titanium sites on the MXene surface. The peak located around 1200–1050 cm^{-1} is assigned to C–F stretching vibrations, originating from residual fluorine terminations retained during the etching process. Furthermore, low-frequency bands between 850 and 600 cm^{-1} are attributed to Ti–O and Ti–C lattice vibrations, confirming the preservation of the Ti–C backbone of MXene.[6–9] Upon gold nanoparticle decoration, the MXene/Au spectrum retains all characteristic MXene bands, indicating that the structural framework of MXene remains intact after modification. Notably, enhanced intensity and slight shifts in the O–H and Ti–O related peaks are observed, suggesting strong interfacial interactions between Au nanoparticles and oxygen-containing functional

groups on the MXene surface. These interactions facilitate stable Au anchoring while maintaining the intrinsic conductivity and layered structure of MXene.[6]

SI. 3. Raman Spectra and X-ray diffraction (XRD) characterization

Raman spectroscopy was employed to further investigate the structural characteristics of MXene and MXene/Au nanocomposites (Fig. S4) using an alpha300 R, Raman Imaging Microscope**.** The Raman spectrum of pristine MXene exhibits characteristic vibrational features associated with $Ti_3C_2T_x$. Three prominent bands located at ~ 215, ~ 368, and ~ 628 cm^{-1}, which are assigned to the in-plane and out-of-plane lattice vibrations of Ti and C atoms in the $Ti_3C_2T_x$ structure.[6] In addition, a low-frequency mode observed at 158 cm^{-1} can be attributed to the E_g-type vibration associated with the layered Ti_3C_2 framework, in good agreement with previously reported Raman spectra of $Ti_3C_2T_x$ MXene.[10–12] Upon Au nanoparticle incorporation, the MXene/Au composite retains the fundamental Raman features of MXene, indicating that the layered crystal structure is preserved. However, a noticeable enhancement in Raman intensity and a slight broadening of the characteristic bands are observed, which can be attributed to strong interfacial interactions between the Au nanoparticles and the MXene surface. This enhancement is likely driven by localized surface plasmon resonance effects of Au, which amplify the Raman scattering of adjacent MXene layers. The absence of additional Raman peaks associated with Au is expected due to its Raman-inactive nature.[6]

X-ray diffraction (XRD) measurements were carried out using a PANalytical Empyrean diffractometer equipped with Cu Kα radiation (λ = 1.5406 Å). Fig. S5 presents the XRD patterns of the pristine MXene and Au/MXene composite materials. Both samples exhibit diffraction features characteristic of $Ti_3C_2T_x$ MXene, with prominent peaks located at approximately ~8.5°, ~16°, and ~25°, corresponding to the (002), (004), and (006) crystallographic planes, respectively. The presence of the low-angle (002) reflection confirms the successful formation of layered MXene with an expanded interlayer spacing, following the selective etching of the parent MAX phase.[6,13] The higher-order (004) and (006) reflections further indicate the retained layered stacking of MXene sheets. A weak diffraction feature observed near ~22° is attributed to TiO_2, which likely originates from partial surface oxidation during the etching or post-processing steps. The broad nature of this TiO_2-related peak, particularly within the low-angle region, reflects the relatively poor crystallinity of MXene, a characteristic commonly reported for chemically etched $Ti_3C_2T_x$ materials.[14–16] In the Au/MXene composite, no distinct diffraction peaks corresponding to metallic Au are observed, which can be attributed to the low loading and nanoscale dispersion of Au on the MXene surface. However, a noticeable reduction in peak intensity within the 2θ range of 15–25° is evident for MXene/Au, indicating structural modulation of the MXene layers upon Au nanoparticle incorporation.[6]

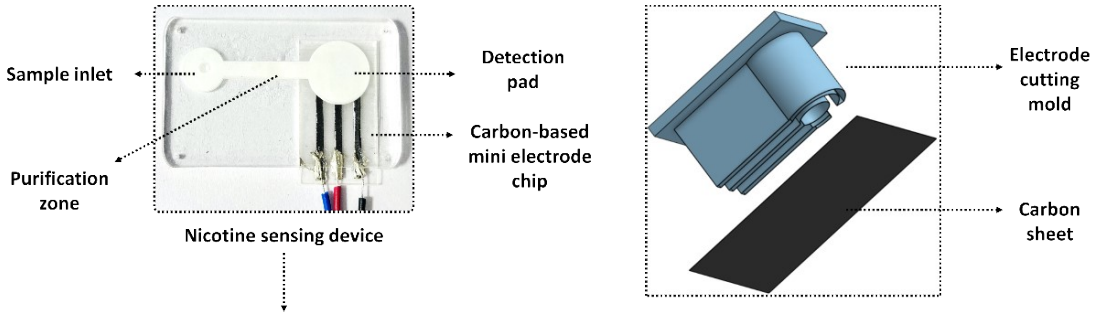

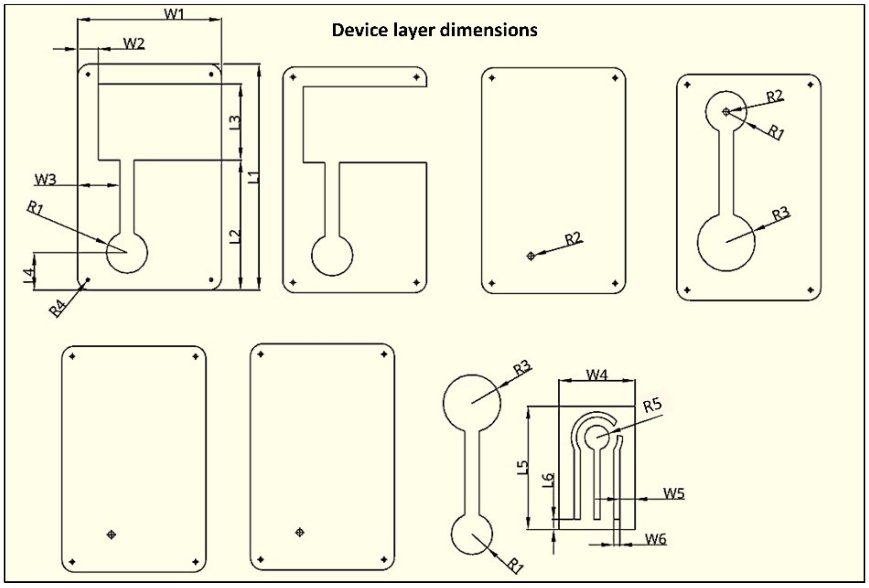

Dimension	(mm)
L1	52
L2	30
L3	10
L4	5
L5	30
L6	1.5
W1	35
W2	4.94
W3	10
W4	18
W5	4.57
W6	1.49
R1	3
R2	1
R3	6
R4	0.8
R5	2

Supporting information 1 Photograph of the assembled nicotine sensing device showing the sample inlet, purification zone, detection pad, and the integrated carbon-based mini electrode chip. (Bottom) Schematic

representation of the microfluidic device layer design with detailed dimensional parameters. The layouts depict the various layers comprising the device including the electrode pattern, fluidic channels, and structural supports. These dimensions ensure precise fabrication and enable effective sample flow, purification, and electrochemical detection within a compact point-of-care platform compatible with lab-on-a-chip applications.

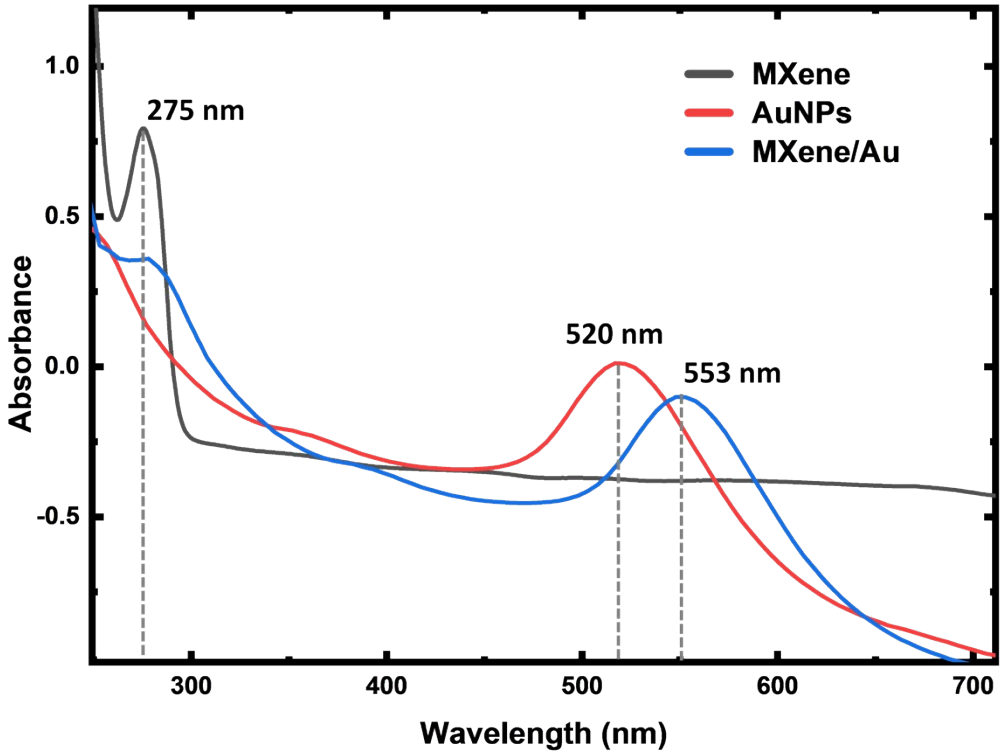

Supporting information 2 UV–VIS absorption spectra of pristine MXene, Au nanoparticles (AuNPs), and the MXene/Au nanocomposite. Pristine MXene (black) exhibits a characteristic absorption band at 275nm, attributed to Ti–C electronic transitions. AuNPs (red) show a distinct surface plasmon resonance (SPR) peak centered around ~520 nm. The MXene/Au (Blue) nanocomposite displays a broadened and slightly shifted SPR band, confirming successful decoration of AuNPs onto the MXene surface and strong interfacial interaction between the two components.[2]

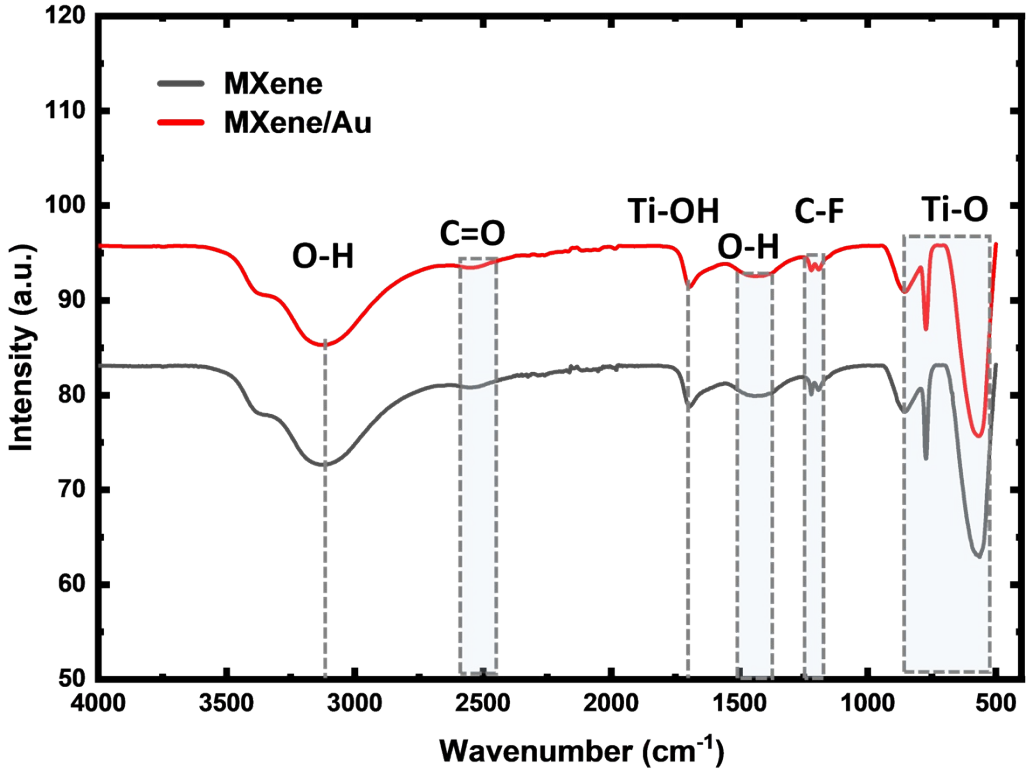

Supporting information 3 Fourier transform infrared (FTIR) spectra of pristine MXene (Black) and MXene/Au (Red).

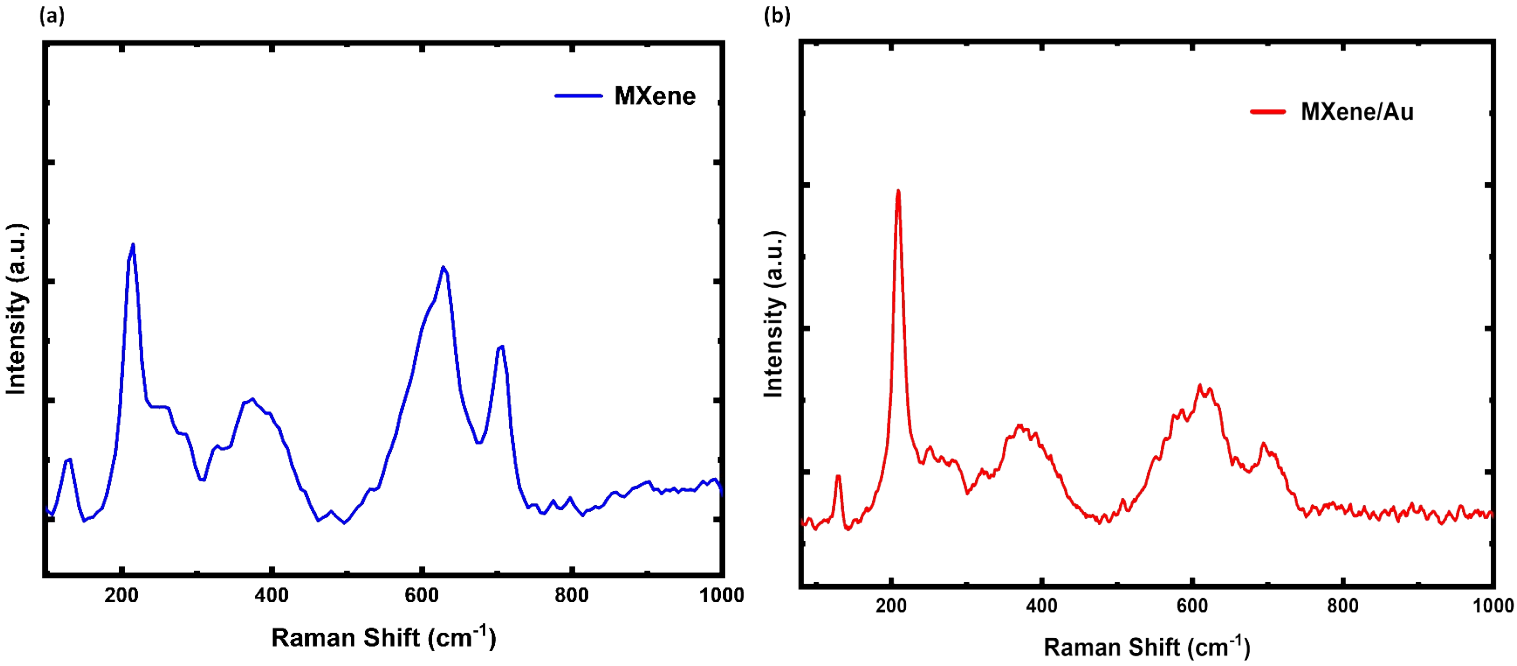

Supporting information 4 Raman spectra of pristine (a) MXene and (b) Au-decorated MXene (MXene/Au).

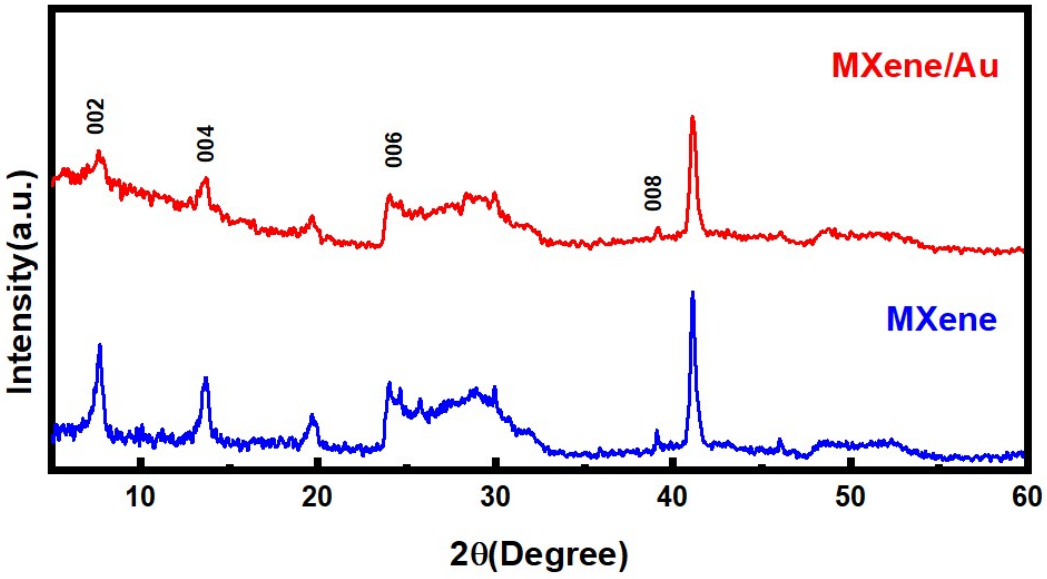

Supporting information 5 X-ray diffraction (XRD) patterns of pristine MXene and Au-decorated MXene (MXene/Au). The characteristic low-angle reflections indexed to the (002), (004), (006), and (008) planes confirm the layered $Ti_3C_2T_x$ structure.

MXene

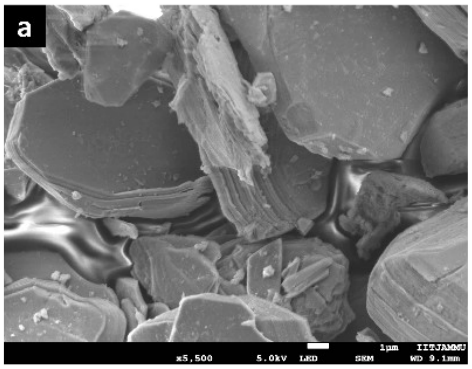

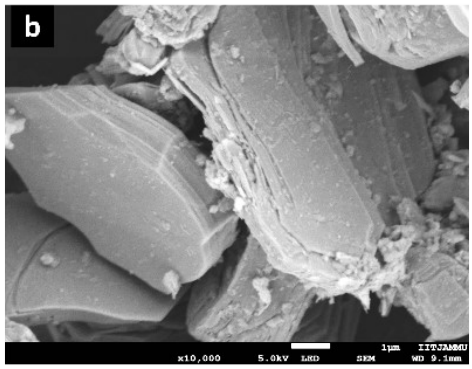

MXene/Au

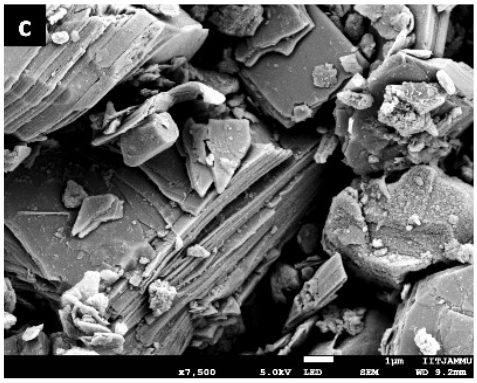

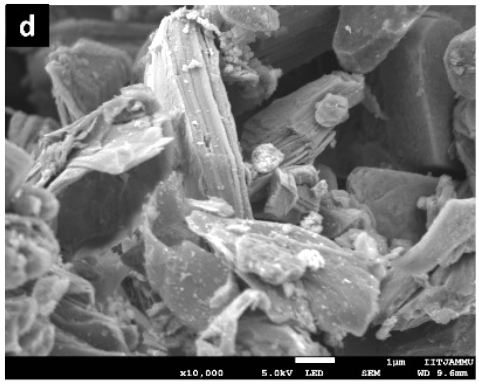

CBME/MXene/Au

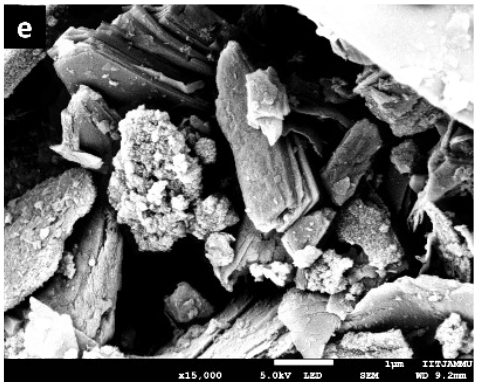

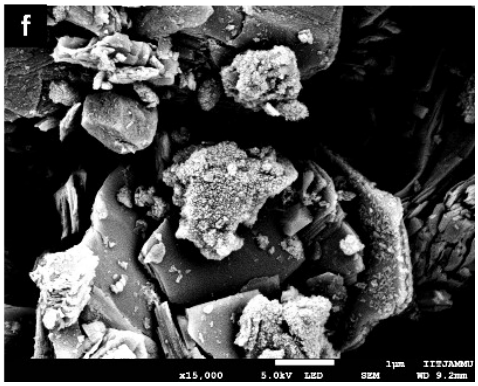

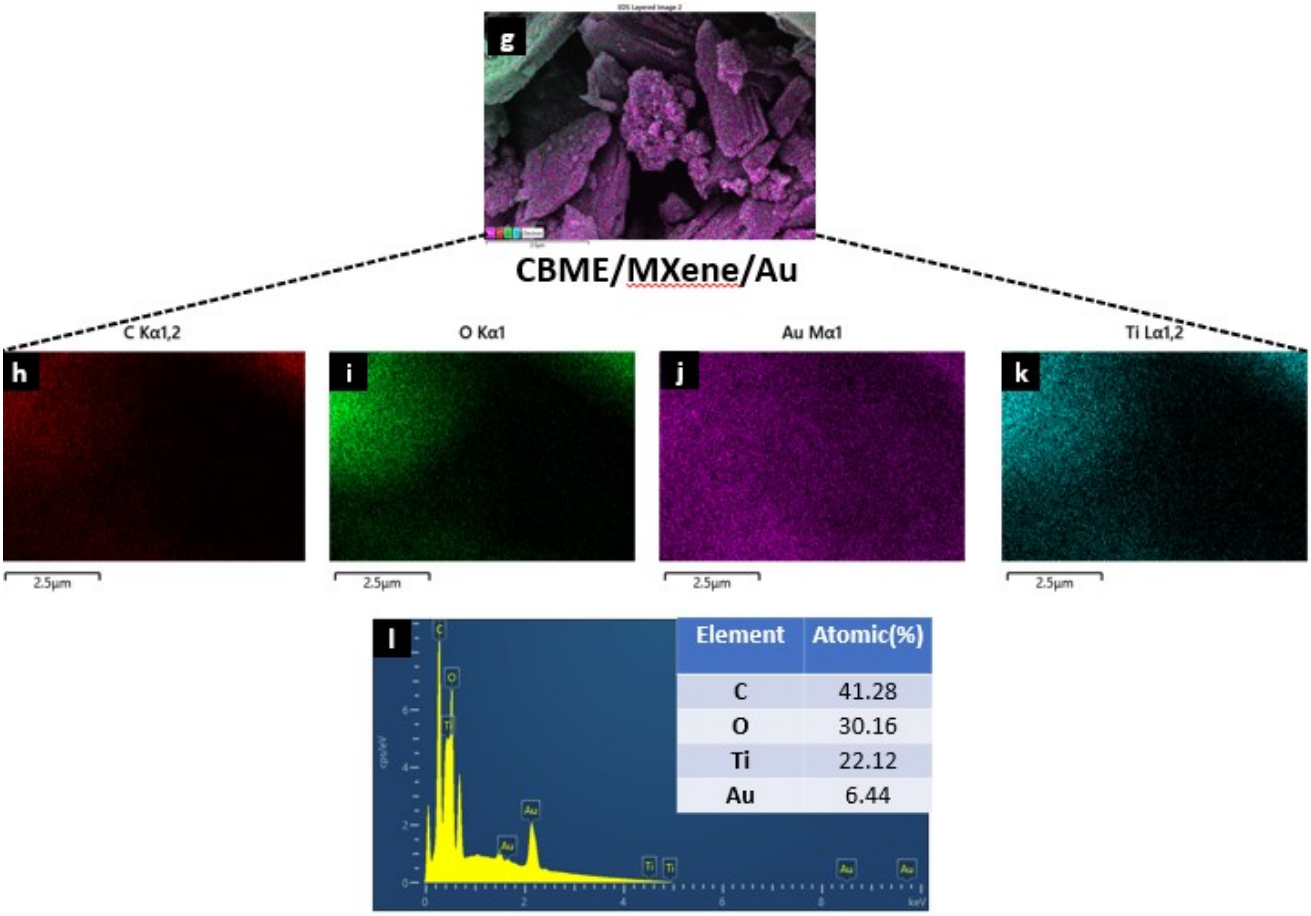

Supporting information 6 Field-Emission scanning electron microscope (FE-SEM) and energy dispersive X-ray spectroscopy (EDS) analysis of the composite material. (a, b) pristine Ti_3C_2 MXene, (c, d) MXene/Au nanocomposite, and (e, f) CBME/MXene/Au-modified carbon-based mini-electrode, illustrating the transition from a layered MXene morphology to Au-decorated, hierarchically rough surfaces and their integration onto the porous carbon substrate, which together enhance electroactive area and facilitate efficient charge transfer. Panel (g) shows the corresponding FE-SEM image of the CBME/MXene/Au surface used for elemental mapping, while (h–k) present energy-dispersive X-ray (EDS) elemental maps for C, O, Au, and Ti, confirming the homogeneous distribution of MXene sheets and well-dispersed Au nanoparticles over the carbon electrode. The EDS spectrum and quantitative analysis in (l) further verify the presence of C, O, Ti, and Au with atomic percentages illustrating their individual distribution across the composite structure.

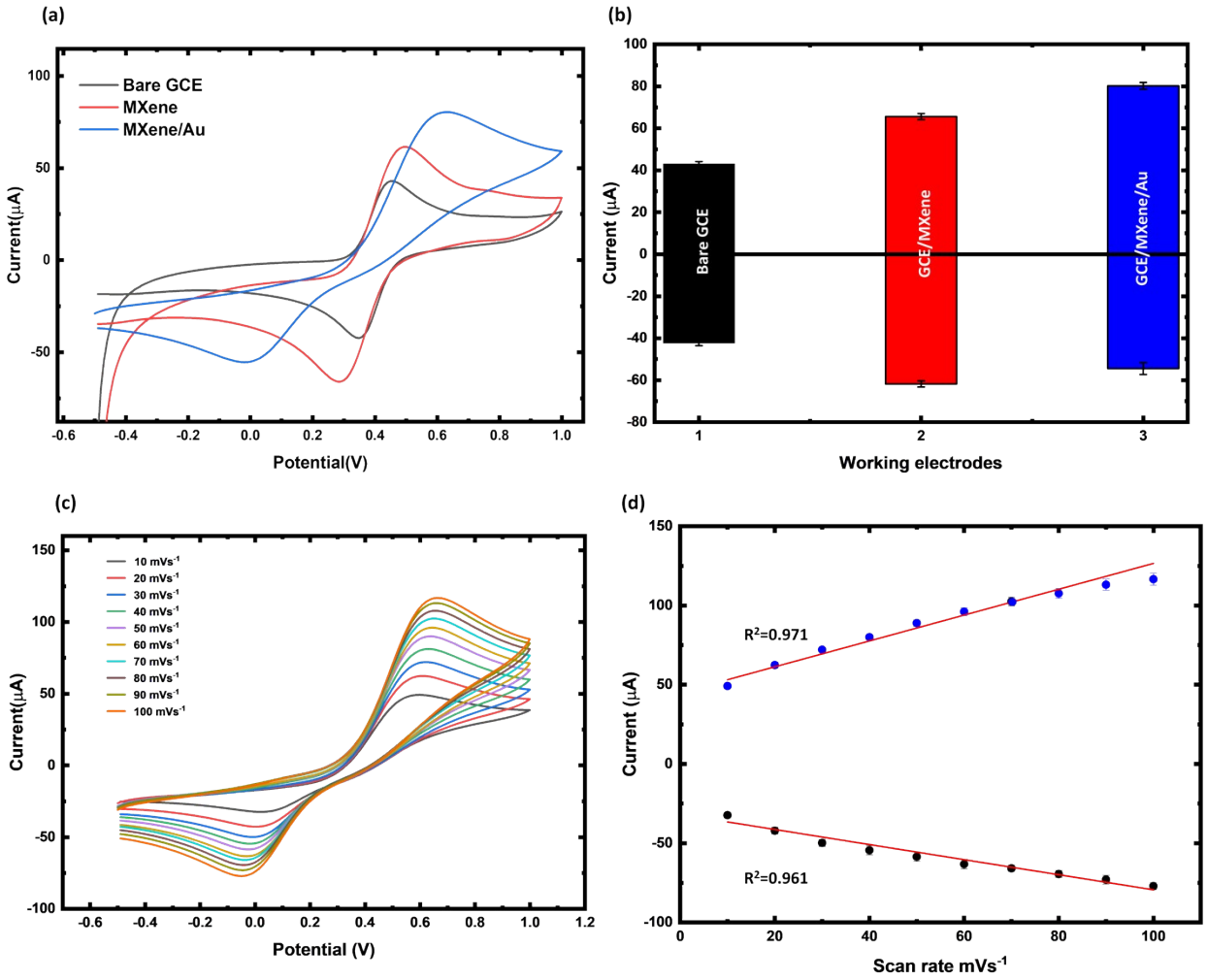

Supporting information 7 Electrochemical characterization of the MXene/gold nanocomposite modified glassy carbon electrode (GCE) for nicotine sensing. (a) Cyclic voltammograms (CV) comparing bare GCE, MXene-modified GCE, and MXene/Au nanocomposite-modified GCE in a standard electrolyte, demonstrating enhanced current response with the nanocomposite. (b) Bar graph showing the peak current responses of different electrode modifications, highlighting the superior electrocatalytic performance of the MXene/Au electrode. (c) CV scans of the MXene/Au modified electrode at varying scan rates (10–100 mV/s), indicating scan rate-dependent current response. (d) Linear relationship between oxidation (positive peak) and reduction (negative peak) peak currents and the square root of the scan rate, confirming diffusion-controlled electrochemical behavior with correlation coefficients (R^2) of 0.975 and 0.962, respectively. error bars represent the standard deviation (±SD) derived from three independent experimental replicates (n = 3), ensuring the reproducibility and statistical reliability of the measured data.

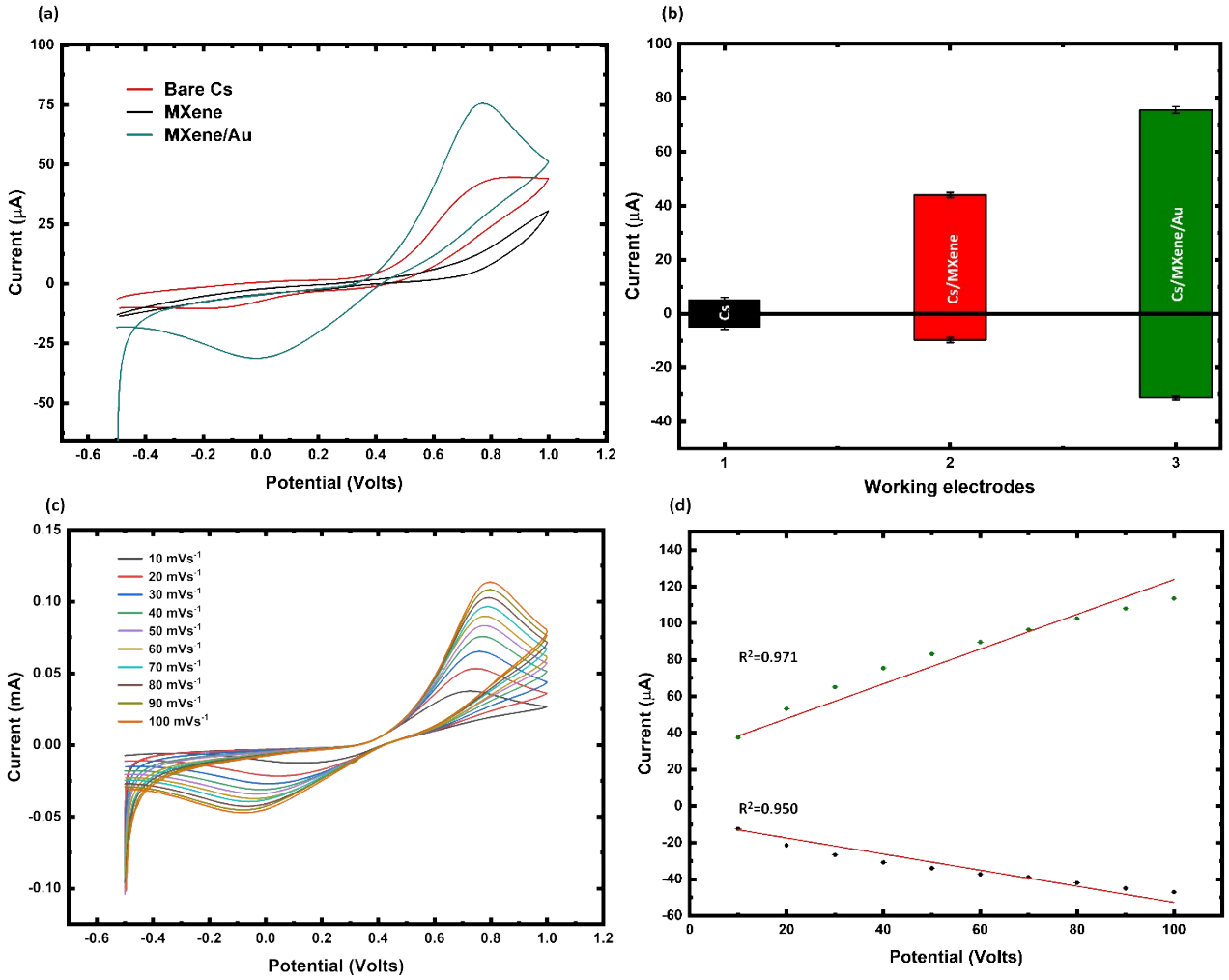

Supporting information 8 Electrochemical performance of MXene/Au nanocomposite modified carbon sheet (Cs) electrodes. (a) Cyclic voltammograms (CV) comparing bare Cs, MXene/Cs, and MXene/Au/electrodes, demonstrating enhanced redox behavior and current response with nanocomposite functionalization. (b) Bar graph showing the peak current responses for each electrode variant, highlighting the superior electrocatalytic activity of the MXene/Au-modified Cs. (c) CVs of the MXene/Au-modified Cs at varying scan rates (10–100 mV/s), illustrating scan rate-dependent current responses. (d) Linear relationship between oxidation and reduction peak currents and scan rate, indicating diffusion-controlled electrochemical processes (R^2 = 0.971 for anodic and R^2 = 0.950 cathodic peaks). Error bars represent the standard deviation derived from three independent replicate measurements.

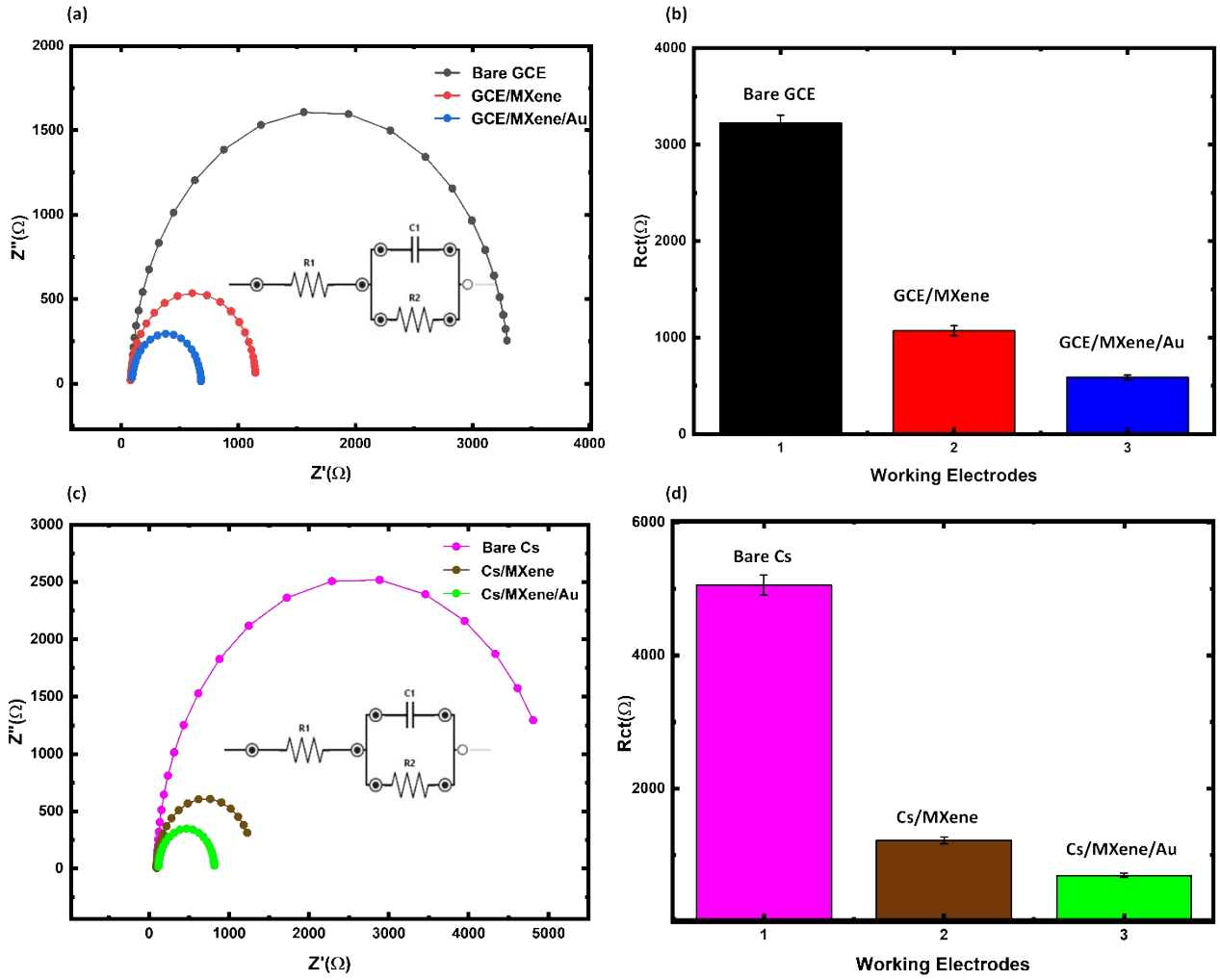

Supporting information 9 Electrochemical impedance spectroscopy (EIS) analysis of electrode modifications. (a) Nyquist plots for bare GCE, GCE/MXene, and GCE/MXene/Au electrodes, with equivalent circuit inset, highlighting reduced charge transfer resistance (Rct) upon nanocomposite functionalization. (b) Bar chart comparing Rct values for the corresponding GCE-based electrodes, showing a significant decrease in Rct for MXene and MXene/Au modifications. (c) Nyquist plots for bare carbon sheet (Cs), Cs/MXene, and Cs/MXene/Au electrodes, with circuit inset, indicating improved electron transfer kinetics after stepwise modification. (d) Bar graph of Rct values for Cs-based electrodes, demonstrating pronounced reduction in Rct for Cs/MXene/Au compared to bare Cs. Error bars denote standard deviations calculated from triplicate measurements.

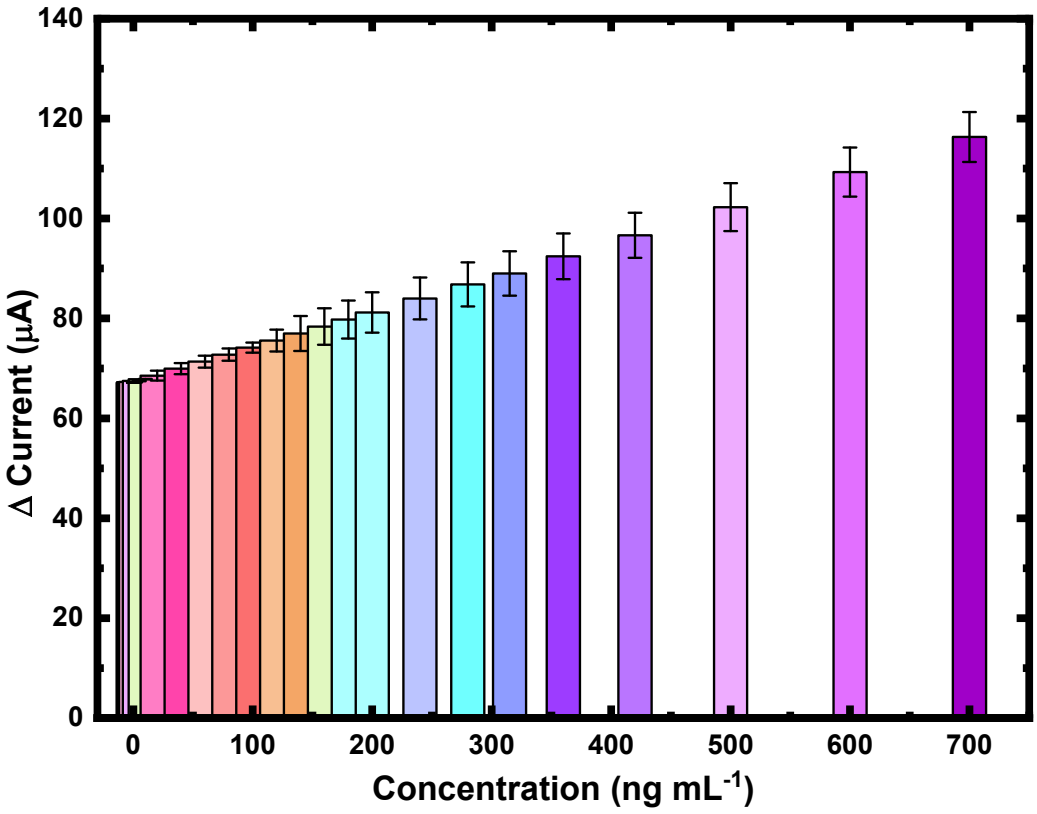

Supporting information 10 Cyclic Voltammetric (CV) response of the Cs/MXene/Au-modified miniaturized electrode for nicotine detection in human saliva spiked with known nicotine concentrations (0–700 ng mL^{-1}). The anodic peak current (ΔI) increased proportionally with rising nicotine concentration, indicating efficient electron transfer kinetics and strong electrochemical sensitivity of the fabricated device in a real biological matrix. Error bars represent standard deviation (n = 3), confirming the reproducibility and analytical reliability of the developed point-of-care sensing platform

Table. S1. Analytical performance of the MXene/Au-modified miniaturized electrode for nicotine detection in spiked human saliva samples. The table summarizes the spiked and calculated nicotine concentrations, standard deviation (STD), recovery percentage, and relative standard deviation (RSD%) for each concentration. The recovery values ranged between 97.7% and 120%, with RSD < 5.0%, indicating high accuracy, reproducibility, and reliability of the developed point-of-care electrochemical sensing platform for quantitative nicotine determination in biological matrices.

Sample	Spiked nicotine(ng/ml)	Calculated nicotine(ng/ml)	STD	Recovery (%)	RSD (%)
1	0.1	0.12	0.0013	120.0	1.0833
2	0.15	0.14	0.007	93.33	5.0
3	0.5	0.49	0.024	98.0	4.9
4	1	1.2	0.06	120.0	5.0
5	2	2.02	0.082	101.0	4.06
6	5	5.01	0.06	100.2	1.20
7	10	10.01	0.042	100.1	0.42
8	20	19.91	0.99	99.55	4.97
9	40	39.08	1.1	97.7	2.82
10	60	60.01	1.2	100.02	2.0
11	80	80	1.24	100.0	1.55
12	100	100	1	100.0	1.0
13	120	120	2.2	100.0	1.83
14	140	139.8	3.5	99.86	2.50
15	160	161.6	3.65	101.0	2.26
16	180	180	3.8	100.0	2.11
17	200	200	4.05	100.0	2.03
18	240	241.6	4.2	100.6	1.74
19	280	280	4.4	100.0	1.57
20	315	316.8	4.45	100.57	1.40
21	360	360.03	4.58	100.01	1.27
22	420	420	4.5	100.0	1.07
23	500	500	4.8	100.0	0.96
24	600	599.8	4.92	99.97	0.82
25	700	700.02	5.01	100.00	0.72

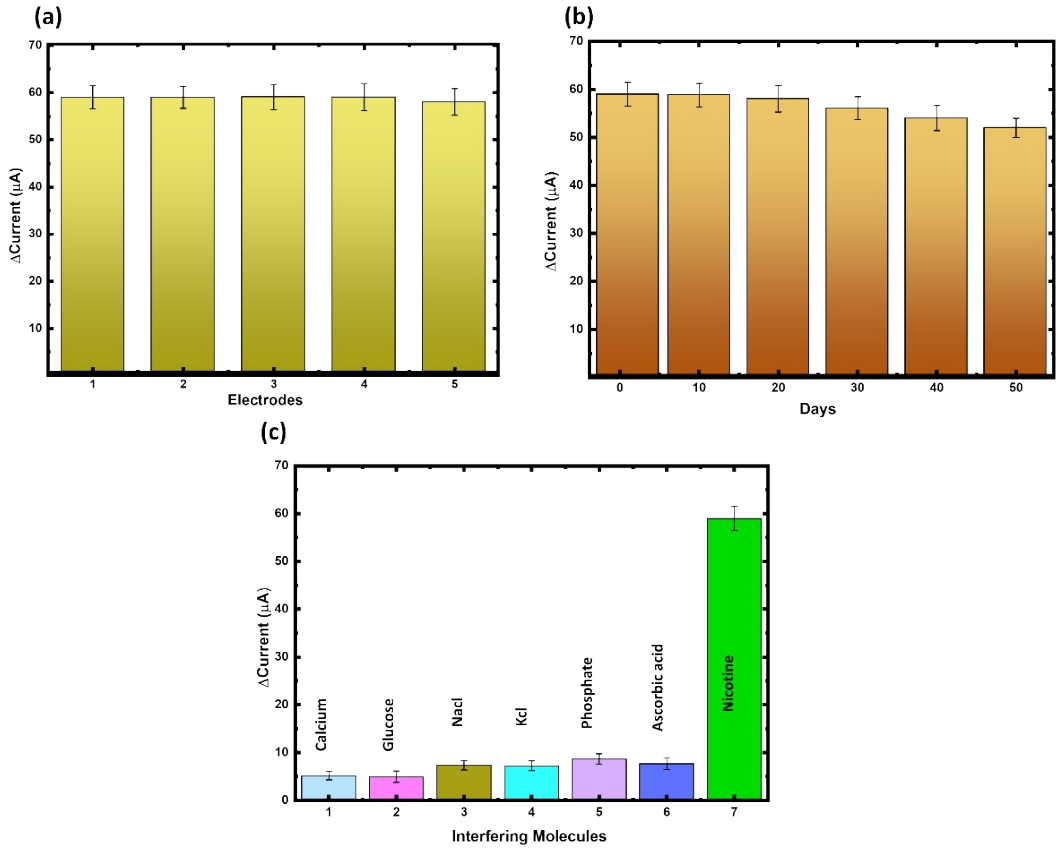

Supporting information 11 (a) Reproducibility analysis of the Cs/MXene/Au-fabricated electrode showing ΔCurrent (μA) responses for five independently prepared electrodes. The current values remained consistent, ranging from 58.03 to 59.07 μA, with standard deviations between 2.33 and 2.84 μA. (b) Long-term stability evaluation of the fabricated electrode over 50 days, illustrating changes in ΔCurrent (μA). The electrode retained stable performance, with only a slight decrease from 59.01 μA on day 1 to 52.02 μA on day 50, indicating strong durability and reproducibility for prolonged electrochemical operation. (c) Selectivity evaluation through interference studies, highlighting a significantly higher current response for nicotine compared to common interfering species, thereby demonstrating high specificity. Error bars represent the standard deviation from triplicate measurements.

References

1 M. Kumari, N. Kumar, S. Kumar, S. Gandhi, E. Zussman and R. K. Arun, *Analytical Methods*, 2024, **16**, 3007–3019.

2 E. Satheeshkumar, T. Makaryan, A. Melikyan, H. Minassian, Y. Gogotsi and M. Yoshimura, 2016, 1–9.

3 M. Elancheziyan, M. Singh and K. Won, *nanomaterials Article*, ,DOI:https://doi.org/10.3390/ nano14201655 Academic.

4 S. M. KuppuSakthi Velu, Alagumalai Manimekalai and and S. S. MohammadAslam,

Prasanta Roy, 2025.

5 Y. Li, X. Zhou, J. Wang, Q. Deng, M. Li and S. Du, 2017, 24698–24708.

6 G. T. M. Kadja, S. A. C. Natalya, F. Balqis, N. J. Azhari, N. Nurdini, A. Sumboja, R. Sri, U. Pratomo and M. Khalil, *Nano-Structures & Nano-Objects*, 2023, **36**, 101059.

7 P. Karthikeyan, S. S. D. Elanchezhiyan, J. Preethi, K. Talukdar, S. Meenakshi and C. Min, *Ceramics International*, 2021, **47**, 732–739.

8 A. Sengupta, B. V. B. Rao, N. Sharma, S. Parmar, V. Chavan, S. K. Singh, S. Kale and S. Ogale, 2020, 8466–8476.

9 U. Pratomo, R. Adhia, A. Pramudya, G. T. M. Kadja, M. Khalil and I. Primadona, *Materials Letters*, 2023, **337**, 133932.

10 J. Rajendran, A. K. Sundramoorthy, D. Ganapathy, R. Atchudan, M. A. Habila and D. Nallaswamy, *Journal of Hazardous Materials*, 2022, **440**, 129705.

11 A. Sarycheva and Y. Gogotsi, .

12 F. Sagita, C. L. Radiman, M. Ledyastuti, M. Khalil and G. T. M. Kadja, .

13 L. Zhang, W. Su, Y. Huang, H. Li, L. Fu, K. Song, X. Huang and J. Yu, .

14 M. Murugesan, K. R. Nagavenkatesh, P. Devendran, N. Nallamuthu, C. Sambathkumar and M. K. Kumar, .

15 Y. He, L. Wang, X. Wang, C. Shen, Q. Hu, A. Zhou and X. Liu, *Journal of Materials Science: Materials in Electronics*, 2020, **31**, 6735–6743.

16 D. Roy, R. Singh, N. Chanda and S. Mandal, *Journal of Applied Electrochemistry*, 2025, **55**, 1045–1058.